Commun. Comput. Phys.
doi: 10.4208/cicp.240111.060811s

Vol. **12**, No. 2, pp. 494-514
August 2012

Dynamical Motion Driven by Periodic Forcing on an Open Elastic Tube in Fluid

Wanho Lee[1], Sookkyung Lim[2] and Eunok Jung[1,*]

[1] *Konkuk University, Department of Mathematics, 1 Hwayang-dong, Gwangjin-gu, Seoul, 143-701, Republic of Korea.*
[2] *University of Cincinnati, Department of Mathematical Sciences, 839 Old Chem, Cincinnati, OH 45221, USA.*

Received 24 January 2011; Accepted (in revised version) 6 August 2011

Available online 20 February 2012

Abstract. We present a three dimensional model of an open elastic tube immersed in fluid to understand valveless pumping mechanism. A fluid-tube interaction problem is simulated by the volume conserved immersed boundary method which prevents the generation of spurious velocity field near the tube and local cluster of the tube surface. In order to explain pumping phenomena without valves, average net flow is measured by changing parameter values such as pumping frequency, compression duration, and pumping amplitude. Some frequencies that make the system reach maximal or minimal net flow are selected to study case by case. We also study the effectiveness of fluid mixing using the Shannon entropy increase rate.

AMS subject classifications: 65-04, 65M06, 76D05, 76M20

Key words: Valveless pumping, volume conserved immersed boundary method, fluid mixing, average net flow.

1 Introduction

Any directional flow driven by pumping without valves in a fluid-structure mechanical system is called valveless pumping (VP). In valveless pump systems, a unidirectional net flow can be generated by applying the periodic force at an asymmetric location of the elastic tube. The closed or open valveless pump systems have been intensively studied for recent decades in computational [1, 3, 4, 8–11, 14, 18–21, 27–29] and experimental settings [4–7, 12, 15–17, 26]. Liebau first presented the results from the initial studies on VP research. In his experiments of VP, both closed and open valveless pump systems were

*Corresponding author. *Email addresses:* lwh3958@konkuk.ac.kr (W. Lee), limsk@math.uc.edu (S. Lim), junge@konkuk.ac.kr (E. Jung)

proposed to explain the VP mechanisms [15–17]. Liebau's closed valveless pump system is composed of two different impedance materials whose elastic properties and radii of tubes are different. In particular, the studies on a closed loop of tubing that consists of two different types of homogeneous materials, soft and (almost) rigid materials, have been comprehensively performed [9, 10, 19, 21, 28]. The macro- and micro-scale experiments have been developed for biological and biomedical applications [7, 26]. There have been also proposed computational models with different space dimensions: zero-dimensional models (compartment models) [4, 9, 20], one-dimensional models [1, 3, 19, 21, 28, 29], two-dimensional [8,10,11,14] and three-dimensional models [8,18,27]. In Liebau's open valveless pump system, he built a model that both ends of an open elastic tube are connected to tanks as reservoirs [15–17] to generate unidirectional net flow. Recently, it has been reported that an open elastic tube made of even a single type of homogeneous material is enough to show VP phenomena [14]. In both open and closed valveless pump systems, the important features have been observed that the direction and the magnitude of a net flow are determined by the driving and geometric parameters of the valveless pump system. The pumping frequency is one of the critical parameters in determining characteristics of VP.

In this work, we have developed a three-dimensional model of an open valveless tube made of a single homogeneous material. This computational model is an extension of our two-dimensional open valveless pump model presented in [14], in which we showed the important features of VP although only one soft material was used: a unidirectional net flow is observed and its direction is very sensitive to pumping frequency. We also investigated that the direction and the magnitude of a net flow can be explained, respectively, by the sign and the amount of the work done over a cycle by a periodic force acting on the elastic tube. Even though a two-dimensional open VP model contributed to revelation of important phenomena of VP including the fluid dynamics and wall motions, there were still spatial limitations on plane. Hence, we extend our two-dimensional model to the three-dimensional model using the volume conserved immersed boundary (IB) method. This method helps to prevent the generation of spurious velocity near the tube and local cluster of the elastic tube boundary. As the earlier research on both the closed and open VP systems reported, the similar features of the systems are observed in our model. In order to demonstrate pumping phenomena, averaged net flow is measured by changing parameter values such as frequency, compression duration, and amplitude of the driving forcing. The case studies with maximal/minimal directional flows and almost zero flows are presented. We also investigate the effectiveness of fluid mixing using the Shannon entropy increase rate and observe that mixing by valveless pumping is very efficient at high Reynolds number [2]. Some selected animations for the motion of fluid dynamics inside and outside of the elastic open tube are presented in [13].

The benefits of valveless pumps are that they can generate significant flows with low power requirements and are easy to manufacture. Especially, open tubes made of a homogeneous material can be easily constructed to generate net flow and fluid mixing at specified pumping frequencies, although the quality of the material may be an issue in

material science. VP systems can therefore be a great tool for the fluid-structure interaction models in many biomedical and engineering applications. For instance, this open VP model can be implemented on a coronary artery bypass graft (CABG) surgery [31]. According to the American Heart Association 427,000 coronary artery bypass graft surgeries were performed in the United States in 2004, making it one of the most commonly performed major operations. CABG surgery creates new routes around narrowed or blocked arteries, allowing sufficient blood flow to deliver oxygen and nutrients to the heart muscle. This simple design of open valveless pump model could provide the efficient pumping during CABG surgery.

The mathematical model of the elastic open tube VP system and the volume conserved IB method are presented in Section 2. In Section 3, the comprehensive numerical results are discussed including the parametric and case studies. Shannon entropy increase rate is also calculated for investigating the flow mixing. Summary and conclusion are addressed in the final section.

2 Mathematical model

In this section, we state a mathematical formulation and a numerical scheme that describe the motion of valveless pumping in an open tube system based on the immersed boundary method. Fig. 1 displays the initial configuration of a computational model. An incompressible viscous fluid fills an entire box and an open elastic tube is embedded in

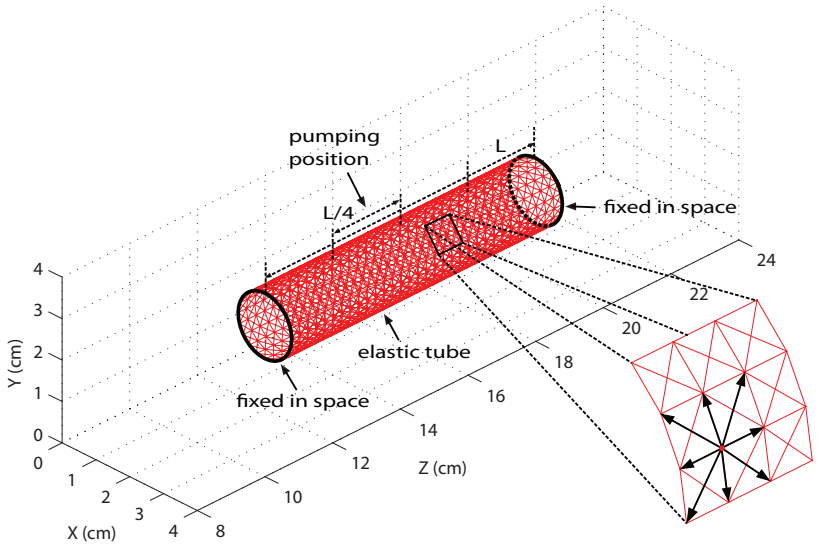

Figure 1: Initial configuration of an open elastic tube immersed in a fluid box. The tube consists of elastic springs that connect material points, each of which is connected to eight adjacent points. Both ends of the tube are fixed in space. The pumping position is located at the second quarter of the elastic tube. L is the length of the elastic tube.

Table 1: Physical parameters.

Parameters	Notation	Values
Fluid density	ρ	$1g/cm^3$
Fluid viscosity	μ	$0.01g/cm\cdot sec$
Computational domain	$L_x\times L_y\times L_x$	$4cm\times 4cm\times 32cm$
Stiffness	κ_t	$2000dyne/cm^3$
Stretch stiffness	κ_s	$200g/sec^2$
Bending coefficient	κ_b	$26.5g\cdot cm^2/sec^2$
Pumping amplitude	a	$0.4\sim 0.8cm$
Frequency	f	$0.05\sim 10Hz$
Compression duration	d	$0.1\sim 1$
Radius of tube	R	$0.8cm$
Length of tube	L	$8cm$

Table 2: Computational parameters.

Parameters	Notation	Values
Duration of simulation	$t_{\max}$	$50sec$
Number of ring boundary points	M_1	80
Number of bar boundary points	M_2	129
Meshwidth	$h=\triangle x=\triangle y=\triangle z$	$0.125cm$
Time step	$\triangle t$	0.001 sec
Fluid grid	$N_x\times N_y\times N_z$	$32\times 32\times 256$

this box. Fluid motion is driven by the asymmetric periodic pumping applied on the second quarter of the elastic tube. Both ends of the elastic tube are fixed in space. The tube wall is composed of elastic springs that link one material point to the eight adjacent material points.

The fluid is treated as Eulerian in which the fluid is defined on a fixed Cartesian coordinate system and the immersed elastic boundary is treated as Lagrangian in which the boundary is defined on a moving curvilinear coordinate system. Physical and computational parameters in CGS units are listed in Table 1 and 2.

2.1 Equations of motion

We first describe fluid equations. Let the fluid velocity be $\boldsymbol{u}(\boldsymbol{x},t)$, the fluid pressure be $p(\boldsymbol{x},t)$, and the fluid force density be $\boldsymbol{f}(\boldsymbol{x},t)$, where $\boldsymbol{x}=(x_1,x_2,x_3)$ are fixed Cartesian coordinates and t is time. Fluid equations are then given as follows:

$$\rho\left(\frac{\partial \boldsymbol{u}}{\partial t}+(\boldsymbol{u}\cdot\nabla)\boldsymbol{u}\right)+\nabla p=\mu\nabla^2\boldsymbol{u}+\boldsymbol{f}, \tag{2.1}$$

$$\nabla\cdot\boldsymbol{u}=0, \tag{2.2}$$

where ρ and μ are the fluid density and viscosity, respectively. Eqs. (2.1) and (2.2) are viscous incompressible Navier-Stokes equations in Eulerian form.

For structure equations, we let (r,s) be moving curvilinear coordinates. The boundary force density $\boldsymbol{F}$ is given by

$$\boldsymbol{F}(r,s,t)=\kappa_t(\boldsymbol{Z}(r,s,t)-\boldsymbol{X}(r,s,t))-\frac{\partial E_{bend}}{\partial \boldsymbol{X}}-\frac{\partial E_{stretch}}{\partial \boldsymbol{X}}, \tag{2.3}$$

which describes the motion of the elastic tube in Lagrangian form. Here, $\boldsymbol{X}(r,s,t)$ is the position of the elastic tube at any time t, $\boldsymbol{Z}(r,s,t)$ is the target position that drives the motion of the elastic tube, and κ_t is stiffness constant. The energy functions, E_{bend} and $E_{stretch}$, are the elastic energy from bending and stretching, respectively. These energy potentials are described in detail as

$$E_{bend}[\boldsymbol{X}]=\frac{1}{2}\kappa_b\int\left|\frac{\partial^2\boldsymbol{X}}{\partial s^2}\right|^2 drds, \tag{2.4}$$

$$E_{stretch}[\boldsymbol{X}]=\frac{1}{2}\kappa_s\int\left(\left|\frac{\partial\boldsymbol{X}}{\partial s}\right|-1\right)^2 drds, \tag{2.5}$$

where parameters κ_b and κ_s are bending and stiffness coefficients for the elastic boundary, respectively. The variational derivative $\frac{\partial E}{\partial \boldsymbol{X}}$ of the energy functional $E[\cdot]$ is defined as follows:

$$\lim_{\epsilon\to 0}\frac{d}{d\epsilon}E[\boldsymbol{X}+\epsilon\boldsymbol{Y}]=\int-\frac{\partial E}{\partial \boldsymbol{X}}(r,s,t)\cdot\boldsymbol{Y}(r,s,t)drds, \tag{2.6}$$

where $\epsilon\boldsymbol{Y}$ is the amount of perturbation of the configuration $\boldsymbol{X}$. Hence, we can obtain bending and stretching force densities in the following way:

$$\boldsymbol{F}_{bend}=-\frac{\partial E_{bend}}{\partial \boldsymbol{X}}=-\kappa_b\frac{\partial^4\boldsymbol{X}}{\partial s^4}, \tag{2.7}$$

$$\boldsymbol{F}_{stretch}=-\frac{\partial E_{stretch}}{\partial \boldsymbol{X}}=\frac{\partial}{\partial s}(\boldsymbol{T}\boldsymbol{\tau}), \tag{2.8}$$

where

$$\boldsymbol{T}=\kappa_s\left(\left|\frac{\partial\boldsymbol{X}}{\partial s}\right|-1\right), \tag{2.9}$$

$$\boldsymbol{\tau}=\frac{\partial\boldsymbol{X}}{\partial s}\Big/\left|\frac{\partial\boldsymbol{X}}{\partial s}\right|. \tag{2.10}$$

Here, $\boldsymbol{T}$ is the tension derived from Hooke's law and $\boldsymbol{\tau}$ is the unit tangent vector along the linear spring. Finally, equations that describe the interaction between the fluid and the elastic boundary are as follows:

$$\boldsymbol{f}(\boldsymbol{x},t)=\int\boldsymbol{F}(r,s,t)\delta(\boldsymbol{x}-\boldsymbol{X}(r,s,t))drds, \tag{2.11}$$

$$\frac{\partial\boldsymbol{X}(r,s,t)}{\partial t}=\boldsymbol{U}(r,s,t)=\int\boldsymbol{u}(\boldsymbol{x},t)\delta(\boldsymbol{x}-\boldsymbol{X}(r,s,t))d\boldsymbol{x}, \tag{2.12}$$

where $\boldsymbol{U}(r,s,t)$ is the interpolated velocity of the elastic tube. Both equations involve a three-dimensional Dirac δ-function. Eq. (2.11) describes the relationship between the fluid force density $\boldsymbol{f}(\boldsymbol{x},t)$ and the boundary force density $\boldsymbol{F}(r,s,t)$. Eq. (2.12) is the no-slip condition for a viscous fluid applied at the tube surface, which constrains the immersed boundary to move at the local fluid velocity. Each of the interaction equations takes the form of an integral transformation in which the kernel is $\delta(\boldsymbol{x}-\boldsymbol{X}(r,s,t))$.

To apply a periodic force on the elastic tube the boundary points are tethered to target points whose positions are prescribed in time and space. The elastic tube consists of two parts, pumping and non-pumping. The target position of the non-pumping part remains as the initial position during whole simulation. However, the target position of the pumping part of the tube changes by way of cosine function with one period in space and time as follows:

$$\boldsymbol{A}(r,s,t)=\begin{cases} \dfrac{a}{4}\cos\left(\dfrac{2\pi t}{dP}\right)\cos\left(\dfrac{2\pi(z_0(r,s)-0.375L_z)}{0.25L_z}\right), & \text{if } 0\le \mathrm{mod}(t,P)\le dP, \\ 0, & \text{if } dP\le \mathrm{mod}(t,P)\le P, \end{cases} \tag{2.13}$$

where a is the pumping amplitude, z_0 is the component of the position of the tube in z-direction at $t=0$, and P denotes the period; i.e., $f=\frac{1}{P}$ is the frequency of oscillations. dP is the duration of compression, where $0\le d\le 1$, and the function $\boldsymbol{A}(r,s,t)$ remains zero for the time $(P-dP)$ of the period. L_α is the length of the computational domain $[0,L_x]\times[0,L_y]\times[0,L_z]$ in each direction, where $\alpha=x,y,z$. The three components of the time-dependent target position are described by

$$\boldsymbol{Z}_x(r,s,t)=(R-\boldsymbol{A}(r,s,t))\cos\theta+0.5L_x, \tag{2.14}$$

$$\boldsymbol{Z}_y(r,s,t)=(R-\boldsymbol{A}(r,s,t))\sin\theta+0.5L_y, \tag{2.15}$$

$$\boldsymbol{Z}_z(r,s,t)=z_0(r,s), \tag{2.16}$$

where $0\le\theta<2\pi$ and R is the radius of the tube. Note that the pumping force is applied only on the second quarter of the elastic tube.

2.2 Numerical method

In order to solve Eqs. (2.1)-(2.3) and Eqs. (2.11)-(2.12) numerically, we begin with a description of the numerical procedure for the typical IB method. The volume conserved IB method will be presented later on.

Let the tube wall be discretized by material points indicated by (k_1,k_2), where k_1 and k_2 represent point indices in longitudinal and circular directions, respectively. Then we calculate the boundary force density $\boldsymbol{F}^n_{\boldsymbol{k_1,k_2}}$ at each material point $\boldsymbol{X}_{k_1,k_2}$ at time level n. Given configuration $\boldsymbol{X}^n$,

$$\boldsymbol{F}^n_{k_1,k_2}=\kappa_t(\boldsymbol{Z}^n_{k_1,k_2}-\boldsymbol{X}^n_{k_1,k_2})-\boldsymbol{B}\boldsymbol{F}^n_{k_1,k_2}+\boldsymbol{S}\boldsymbol{F}^n_{k_1,k_2}, \tag{2.17}$$

where $\boldsymbol{BF}$ and $\boldsymbol{SF}$ represent bending and stretching force densities, respectively. The bending force exists in two directions, longitudinal and circular. The stretching force exists in four directions, longitudinal, circular, left- and right-handed helical. We will show how to evaluate bending and stretching force densities in the longitudinal direction. The same procedure will be applied for springs in different directions.

Bending and stretching force densities at each material point are evaluated by

$$\boldsymbol{BF}^n_{k_1,k_2} = \kappa_b \frac{\boldsymbol{X}^n_{k_1+2,k_2} - 4\boldsymbol{X}^n_{k_1+1,k_2} + 6\boldsymbol{X}^n_{k_1,k_2} - 4\boldsymbol{X}^n_{k_1-1,k_2} + \boldsymbol{X}^n_{k_1-2,k_2}}{(\Delta s)^4}, \tag{2.18}$$

$$\boldsymbol{SF}^n_{k_1,k_2} = (T_+\boldsymbol{\tau}_+ - T_-\boldsymbol{\tau}_-)/\Delta s, \tag{2.19}$$

where

$$T_+ = \kappa_s \left(\left| \frac{\boldsymbol{X}^n_{k_1+1,k_2} - \boldsymbol{X}^n_{k_1,k_2}}{\Delta s} \right| - 1 \right), \tag{2.20}$$

$$\boldsymbol{\tau}_+ = \left(\frac{\boldsymbol{X}^n_{k_1+1,k_2} - \boldsymbol{X}^n_{k_1,k_2}}{\Delta s} \right) \Bigg/ \left| \frac{\boldsymbol{X}^n_{k_1+1,k_2} - \boldsymbol{X}^n_{k_1,k_2}}{\Delta s} \right|, \tag{2.21}$$

$$T_- = \kappa_s \left(\left| \frac{\boldsymbol{X}^n_{k_1,k_2} - \boldsymbol{X}^n_{k_1-1,k_2}}{\Delta s} \right| - 1 \right), \tag{2.22}$$

$$\boldsymbol{\tau}_- = \left(\frac{\boldsymbol{X}^n_{k_1,k_2} - \boldsymbol{X}^n_{k_1-1,k_2}}{\Delta s} \right) \Bigg/ \left| \frac{\boldsymbol{X}^n_{k_1,k_2} - \boldsymbol{X}^n_{k_1-1,k_2}}{\Delta s} \right|. \tag{2.23}$$

Once we know the boundary force density, a smoothed version of the Dirac-delta function is employed to spread this boundary force to the fluid grid,

$$\boldsymbol{f}^n_{i,j,k} = \sum_{k_1,k_2} \boldsymbol{F}^n_{k_1,k_2} \delta^3_h \left(\boldsymbol{x}_{i,j,k} - \boldsymbol{X}^n_{k_1,k_2} \right) \Delta r \Delta s, \tag{2.24}$$

where $\boldsymbol{x}_{i,j,k} = (ih, jh, kh)$ is a Cartesian grid, h is meshwidth, and (i,j,k) is an integer-valued vector, where $1 \le i \le N_x$, $1 \le j \le N_y$, $1 \le k \le N_z$. A smoothed approximation, δ^3_h, to the three-dimensional Dirac delta function is a product of three one-dimensional delta functions,

$$\delta^3_h(\boldsymbol{x}) = \frac{1}{h^3} \phi\left(\frac{x_1}{h}\right) \phi\left(\frac{x_2}{h}\right) \phi\left(\frac{x_3}{h}\right), \tag{2.25}$$

where the function ϕ is defined by

$$\phi(r) = \begin{cases} \dfrac{3 - 2|r| + \sqrt{1 + 4|r| - 4r^2}}{8}, & \text{if } |r| \le 1, \\ \dfrac{5 - 2|r| - \sqrt{-7 + 12|r| - 4r^2}}{8}, & \text{if } 1 \le |r| \le 2, \\ 0, & \text{if } 2 \le |r|. \end{cases} \tag{2.26}$$

With $\boldsymbol{f}^n$ known, consider the following discretized Navier-Stokes equations:

$$\rho\left(\frac{\boldsymbol{u}^{n+1}-\boldsymbol{u}^n}{\Delta t}+\boldsymbol{u}^n\cdot D^{\pm}\boldsymbol{u}^n\right)+\boldsymbol{D}^0 p^{n+1}=\mu\sum_{k=1,2,3}D_k^+D_k^-\boldsymbol{u}^{n+1}+\boldsymbol{f}^n, \tag{2.27}$$

$$\boldsymbol{D}^0\cdot\boldsymbol{u}^{n+1}=0, \tag{2.28}$$

where D^+, D^-, and $\boldsymbol{D}^0$ represent forward, backward, and centered difference operators, defined in the standard way on a regular Cartesian grid of spacing h, respectively. Therefore, $\boldsymbol{D}^0$ is the central difference approximation to gradient ∇, and $\sum_{k=1,2,3}D_k^+D_k^-$ is a difference operator that approximates the Laplace operator Δ. The upwind scheme is used for $D^{\pm}\boldsymbol{u}$ explicitly. Among the difference operators the central difference operator $\boldsymbol{D}^0$ will be modified below to improve volume conservation of the method. Now we solve the Discrete Navier-Stokes equations using Fast Fourier Transform (FFT) to update fluid velocity and fluid pressure. The local averaged fluid velocity allows us to update the position of the configuration in the following way:

$$\boldsymbol{X}_{k_1,k_2}^{n+1}=\boldsymbol{X}_{k_1,k_2}^n+\Delta t\sum_{i,j,k}\boldsymbol{u}_{i,j,k}^{n+1}\delta_h^3(\boldsymbol{x}_{i,j,k}-\boldsymbol{X}_{k_1,k_2}^n)h^3. \tag{2.29}$$

This completes the numerical procedure of the method.

The typical IB method described above can handle easily the interaction between the fluid and the elastic boundary. However, it loses volume particularly for a closed boundary because the fluid leaks through the wall when the boundary does not maintain its intended shape. To reduce this volume loss, we employed the volume conserved IB method introduced by [25]. In [25], a new difference operator was constructed to replace the central difference operator $\boldsymbol{D}^0$ described in Eqs. (2.27)-(2.28). This new difference operator $\boldsymbol{D}=(D_1,D_2,D_3)$ is tuned to the regularized delta function, δ_h, and is defined as follows:

$$(\boldsymbol{D}\cdot\boldsymbol{u})(\boldsymbol{x})=\frac{1}{h^3}\int_{B(\boldsymbol{x})}(\nabla\cdot\boldsymbol{U})d\boldsymbol{X}, \tag{2.30}$$

where $\boldsymbol{x}=(x_1,x_2,x_3)$ and $B(\boldsymbol{x})$ is a cubic box of side h, i.e.,

$$B(\boldsymbol{x})=\left(x_1-\frac{h}{2},\,x_1+\frac{h}{2}\right)\times\left(x_2-\frac{h}{2},\,x_2+\frac{h}{2}\right)\times\left(x_3-\frac{h}{2},\,x_3+\frac{h}{2}\right). \tag{2.31}$$

$\boldsymbol{U}$ is the interpolated velocity field of the configuration $\boldsymbol{X}$ that is continuous and has continuous first derivatives because of the properties of δ_h. Thus, $\boldsymbol{D}\cdot\boldsymbol{u}$ at the grid point $\boldsymbol{x}$ is the average of $\nabla\cdot\boldsymbol{U}$ over the box $B(\boldsymbol{x})$ centered on $\boldsymbol{x}$. Each component of the operator can be rewritten as

$$(D_1\psi)(x_1,x_2,x_3)=\sum_{(x_1',x_2',x_3')}\psi(x_1',x_2',x_3')\gamma(x_1-x_1')\omega(x_2-x_2')\omega(x_3-x_3'), \tag{2.32}$$

$$(D_2\psi)(x_1,x_2,x_3)=\sum_{(x_1',x_2',x_3')}\psi(x_1',x_2',x_3')\omega(x_1-x_1')\gamma(x_2-x_2')\omega(x_3-x_3'), \tag{2.33}$$

$$(D_3\psi)(x_1,x_2,x_3)=\sum_{(x_1',x_2',x_3')}\psi(x_1',x_2',x_3')\omega(x_1-x_1')\omega(x_2-x_2')\gamma(x_3-x_3'), \tag{2.34}$$

where

$$\gamma(x)=\delta_h(x+X)\Big|_{X=-h/2}^{X=h/2}, \tag{2.35}$$

$$\omega(x)=\int_{-h/2}^{h/2}\delta_h(x+X)dX. \tag{2.36}$$

Here, γ plays a role as a coefficient of a difference operator and ω plays a role as a coefficient of an averaging operator. We can then use these operators for the discrete divergence and the discrete gradient as follows:

$$\boldsymbol{D}\cdot\boldsymbol{u}=D_1u+D_2v+D_3w, \tag{2.37}$$

$$\boldsymbol{D}\psi(\boldsymbol{x})=((D_1\psi)(\boldsymbol{x}),(D_2\psi)(\boldsymbol{x}),(D_3\psi)(\boldsymbol{x})). \tag{2.38}$$

The new operator makes the interpolated velocity field nearly divergence-free. For detailed description of the volume conserved IB method, the reader is referred to [25].

To validate the volume conserved IB method, we considered a simple closed curve (a circle) in two-dimensional space as an elastic boundary immersed in a fluid. The size of the computational domain was $2cm$ in each direction and the number of grid points in each direction was 128. The elastic force from the boundary configuration was generated by

$$\boldsymbol{F}(s,t)=\kappa_c\left(\frac{\partial^2\boldsymbol{X}(s,t)}{\partial s^2}\right), \tag{2.39}$$

where $\kappa_c=50g\cdot cm/sec^2$ was selected for stiffness constant. In this simulation, the parameter values for ρ and μ were used as the same as in Table 1 and total simulation time was $2sec$.

Fig. 2 shows the comparison of the typical IB method with the volume conserved IB method. The left panel shows the boundary configurations at $t=2sec$ and the right panel shows rates of change in volume during simulated time. As seen in Fig. 2, the circle shrinks when the typical IB method was used and hence volume losses about 32%. On the other hand, when the volume conserved IB method was used the boundary configuration remains indistinguishable from the initial state and the volume is well-maintained.

In addition to the two-dimensional experiments for comparison of two methods described above, we considered a three-dimensional open tube immersed in a cuboid as introduced in Section 2 and compared the shape of the tube wall and the velocity fields near the tube of the typical IB method with those of the volume conserved IB method. Fig. 3 shows the velocity vector fields on the plane $z=16cm$ (see Fig. 1) at a given time $t=0.1sec$ when the tube wall contracts. The left and right panels illustrate the velocity vector fields computed from the typical IB method and the volume conserved IB method, respectively. In each panel, the outer circle represents the elastic boundary and the inner circle represents the target position where the elastic boundary follows. It is clear that the velocity vectors from the volume conserved IB method point toward the center in a regular way unlike the typical IB method.

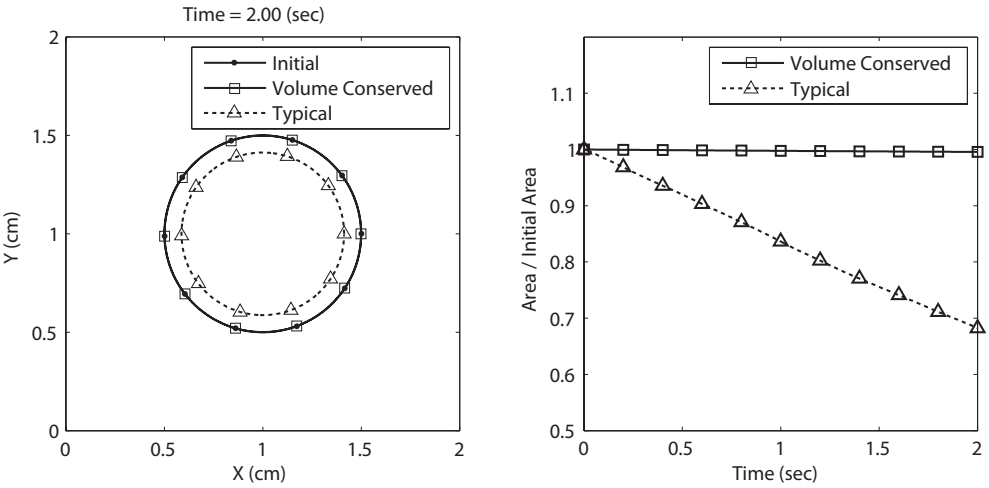

Figure 2: Comparison of the typical IB method with the volume conserved IB method. Left: boundary configurations at $t=2sec$. Right: rates of change in volume during simulated time.

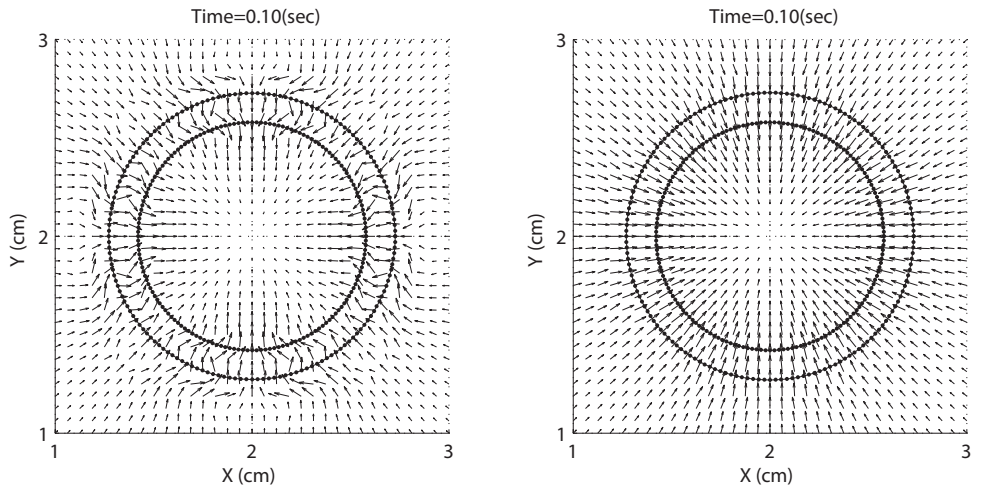

Figure 3: Velocity vector fields on the plane $z=16cm$ at $t=0.1sec$, the time when the tube wall contracts. Left: velocity field computed from the typical IB method. Right: velocity field computed from the volume conserved IB method. The outer circle represents the elastic open tube and the inner circle represents the target position of the tube.

Fig. 4 displays pumping part of tubes at time $t=50sec$ computed from the typical IB method (left panel) and the volume conserved IB method (right panel). In the typical IB method when pumping force is applied periodically, the discrepancy between the pumping part and the non-pumping part is accumulated as simulation time lasts longer. But the volume conserved IB method helps the elastic boundary follow the target position as designated. We can conclude the volume conserved IB method is a more appropriate method for our simulation.

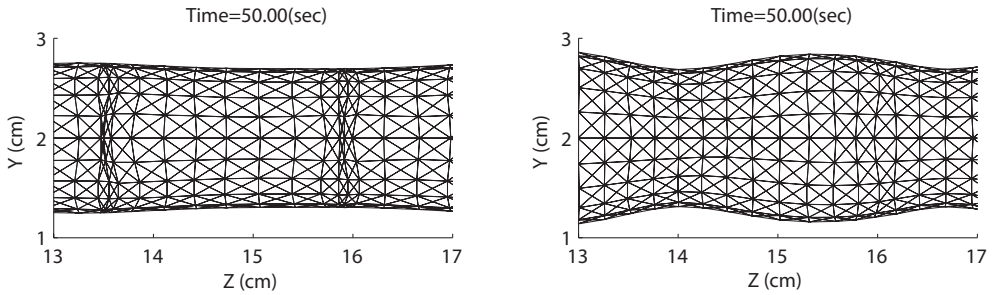

Figure 4: Boundary structures are displayed at $t=50sec$. Left: structure from the typical IB method. Right: structure from the volume conserved IB method.

For convergence study we calculated velocity vector fields on three different grid sizes of m, $2m$, and $4m$, where $2m=32\times32\times256$. The convergence ratios for velocity $\boldsymbol{u}=(u,v,w)$ in the L^2-norm are

$$\frac{||u_m-u_{2m}||_2}{||u_{2m}-u_{4m}||_2}=\frac{||v_m-v_{2m}||_2}{||v_{2m}-v_{4m}||_2}=1.8503, \qquad \frac{||w_m-w_{2m}||_2}{||w_{2m}-w_{4m}||_2}=1.7988. \tag{2.40}$$

All of these ratios are close to 2, which indicates that the numerical scheme is first-order accurate.

3 Results and discussion

In this section, we present the numerical results using the volume conserved IB method. Recall that our computational model is an open elastic tube whose ends are fixed in space and this tube is immersed in a viscous fluid. Average net flow is measured and compared depending on pumping frequency, pumping amplitude, and compression duration. In particular, we investigate three special cases where the average net flow reaches either maximum, minimum, or almost zero values. We also investigate the mixing efficiency of the open valveless pumping model.

After the model reaches the steady state, the average net flow f_{ave} is measured over a circular cross-sectional region inside the tube as follows:

$$f_{ave}=\frac{1}{t_c}\int_0^{t_c}\int_\Gamma w(\boldsymbol{x},t)dAdt, \tag{3.1}$$

where $w(\boldsymbol{x},t)$ is the longitudinal component of a vector field (u,v,w), t_c is the current time, Γ is the circular cross section, and A is the area element. So the average flow can be any real number in which the positive value corresponds to the flow in the positive direction of z-axis, called a *positive flow*. Similarly, the negative value of net flow is called a *negative flow*. The magnitude of net flow will show how much fluid flow is generated by periodic forcing.

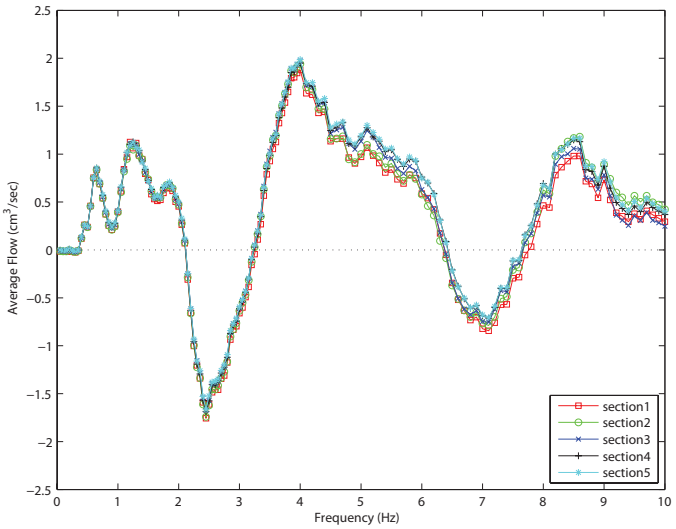

Figure 5: The space- and time-averaged flows measured at five different locations of the tube as functions of frequency are displayed when the compression duration is $d=0.5$, the pumping amplitude is $a=0.64cm$, and the simulated time is $50sec$.

Fig. 5 displays the space- and time-averaged flows measured at five different locations as functions of frequency. In these simulations, compression duration is $d=0.5$, pumping amplitude is $a=0.64cm$, and simulated time is $50sec$. The number of selected pumping frequencies is 140 different values ranging from $0.05Hz$ to $10Hz$. To see whether the average net flow changes with different locations we choose 5 different cross sections of the tube, equally spaced, including both ends of the tube. Fig. 5 demonstrates that the net flow is well maintained in each cross section. Maximum positive flow appears at $f=4Hz$

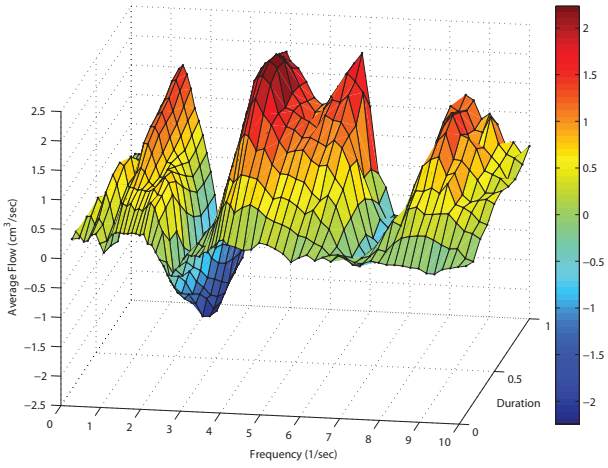

Figure 6: The space- and time-averaged flows as functions of frequency and compression duration are displayed when pumping amplitude is $a=0.64cm$.

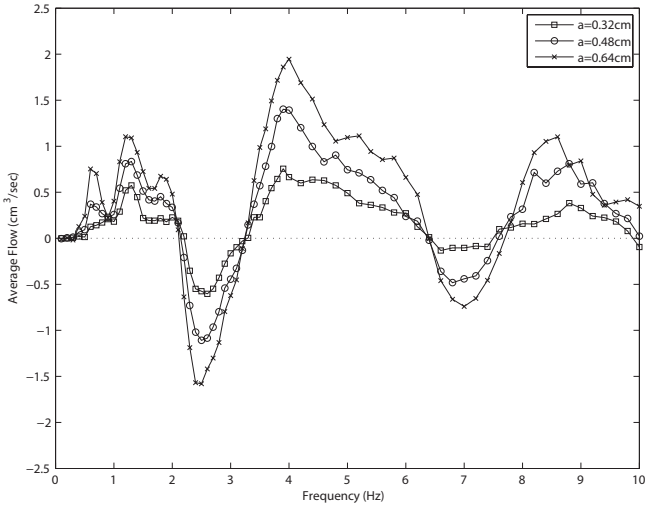

Figure 7: The space- and time-averaged flows as functions of pumping amplitude are displayed when compression duration is $d=0.5$.

and minimum negative flow appears at $f=2.45Hz$. As observed, the pumping frequency plays an important role in determining flow direction and magnitude.

Fig. 6 displays the space- and time-averaged flows as functions of frequency and compression duration. From now on, we will provide average net flow measured at the right end cross section of the tube. Ten different values for compression duration are chosen from 0.1 to 1 with an increment of 0.1 and other parameters such as frequency, pumping amplitude, and simulated time are the same as shown in Fig. 5. We observe that the average net flows are also influenced by the compression duration. The average net flow varies from $-2.2446cm^3/sec$ to $2.2355cm^3/sec$.

Fig. 7 displays the space- and time-averaged flows as functions of pumping amplitude. Pumping amplitude is fixed as $a=0.32cm$, $0.48cm$, and $0.64cm$ and compression duration is fixed as $d=0.5$. It is found that the turning point which changes the flow direction either from a positive flow to a negative flow or vice versa remains the same as pumping amplitude varies. That is, the sign of average net flow is independent of pumping amplitude with all other parameter values held fixed. However, the magnitude of net flow increases as the pumping amplitude increases.

We consider six particular cases when the compression duration is fixed as $d=0.5$ and the pumping amplitude is fixed as $a=0.64cm$ from Fig. 6. The selected cases are two positive flows with local maxima ($f=1.2Hz$, $4Hz$), two almost zero net flows ($f=3.25Hz$, $6.4Hz$), and two negative flows with local minima ($f=2.45Hz$, $7.1Hz$). Pumping frequencies and average net flows corresponding to the six cases are listed in Table 3.

Fig. 8 displays six flow patterns and each panel shows the last 5 cycles after the steady-state is reached. The top row shows two positive flows, the middle row shows two almost zero flows, and the bottom row shows two negative flows. It is shown that for lower

Table 3: Pumping frequency and average net flow.

Status	Frequency	Average net flow
Positive flow	$f=1.2Hz$	$1.0886cm^3/sec$
Positive flow	$f=4Hz$	$1.9867cm^3/sec$
Almost zero flow	$f=3.25Hz$	$0.0505cm^3/sec$
Almost zero flow	$f=6.4Hz$	$0.0765cm^3/sec$
Negative flow	$f=2.45Hz$	$-1.6662cm^3/sec$
Negative flow	$f=7.1Hz$	$-0.7076cm^3/sec$

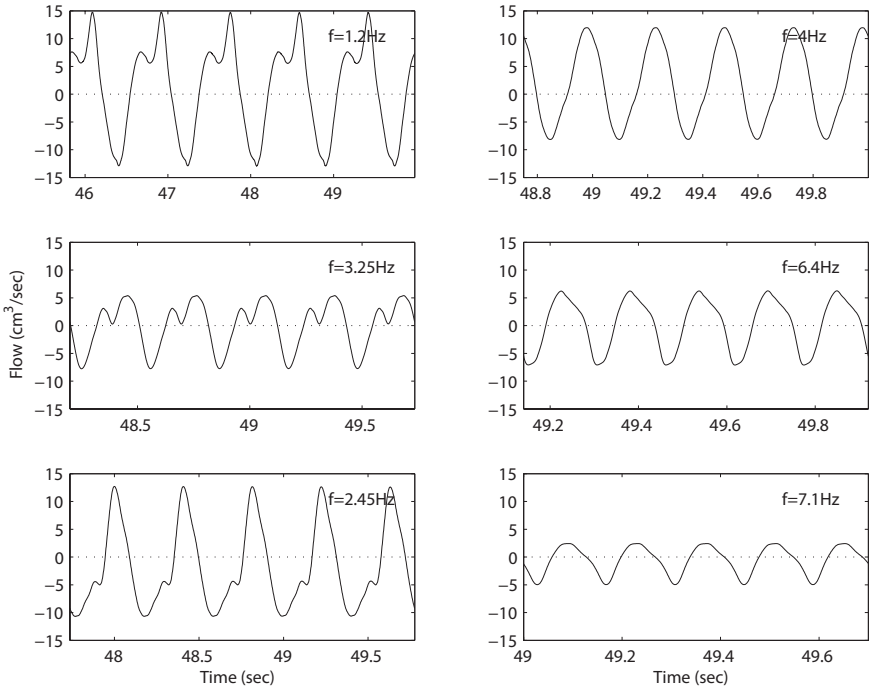

Figure 8: Flow patterns at six different pumping frequencies after the steady-state is reached. Each panel shows the last 5 cycles. The top row shows two positive flows ($f=1.2Hz$, $4Hz$), the middle row shows two almost zero net flows ($f=3.25Hz$, $6.4Hz$), and the bottom row shows two negative flows ($f=2.45Hz$, $7.1Hz$).

frequencies, more oscillations occur during one cycle, see three panels on the left. This is because the backflow generated during the release of compression lasts longer due to low frequency.

Fig. 9 displays a series of snapshots showing the motion of the fluid and tube at five different times t=0sec,5sec,10sec,15sec and 20sec. This is the case where the system generates a positive flow at $f=4Hz$. Fluid markers are initially spread out uniformly inside the tube. As soon as the pumping force is applied at the asymmetric location the tube wall compresses toward the axis of the tube and thus the fluid pumps out of the tube. When the pumping is released the tube wall returns to the initial position which makes the fluid

move inward. Since the amount of the fluid moving outward in positive z-direction during compression is larger than that of the fluid moving inward during release, the overall flow rate takes the positive value. Note that the fluid domain is periodic so that fluid markers leaving the domain on the right side of the tube will reappear on the left side of the fluid domain.

Similarly, Fig. 10 shows the motion of the fluid and tube when the pumping frequency is given at $f=2.45Hz$, in which the system generates a negative flow. The situation is opposite to the case in Fig. 9 because the fluid now flows in the negative z-direction.

In order to measure the mixing performance due to periodic pumping the fluid domain is subdivided into $m=4\times4\times32$ equal cubes. Each cube in right half of the fluid domain in longitudinal direction contains initially 27 particles distributed uniformly inside the cube and this makes the total number of particles in the fluid domain $n_{\text{total}}=27\times m/2$. We introduce the Shannon entropy increase rate, κ, which measures the loss of information in the system with respect to the initial information [2]. The value of κ is evaluated by

$$\kappa=\frac{S-S_0}{S_{\max}-S_0}, \tag{3.2}$$

where S_0 is the entropy of the initial state, $S_{\max}=\log(m)$, and the mixing entropy S is given by

$$S=\frac{-1}{n_{\text{total}}}\sum_{i=1}^{m}n_i\log\frac{n_i}{n_{\text{total}}}, \tag{3.3}$$

where n_i is the number of particles in cube i counted at given time. Note that $S_{\max}$ depends only on the total number of cubes while each cube on the whole domain has the same number of particles so that S_0 is different from $S_{\max}$.

Fig. 11 displays the time evolution of the entropy increase rate for a range of pumping frequencies. Near $t=0$ the entropy increase rate remains zero because the particles stay in the same cube although they are moving back and forth inside the cube. As time goes on, the entropy rate increases in general.

Fig. 12 displays the time evolution of the entropy increase rate as fluid viscosity varies. In these simulations, we fix the pumping frequency as $f=2.45Hz$. The change in fluid viscosity values will lead to the change in the Reynolds number in such a way that the lower the fluid viscosity is, the larger the Reynolds number is. For fluid viscosity $\mu\leq0.01$, the entropy rate increases significantly in time, which means the fluid is well mixed in the end. However, for $\mu\geq1$, the entropy rate does not change much in time, which means the mixing performance is poor. This is because the tube wall in high viscous fluid does not follow well its target position as intended due to viscous drag, and hence the fluid motion is reduced. This becomes clear in Fig. 13.

Fig. 13 shows the performance of the fluid mixing with two different fluid viscosity values when the pumping frequency is fixed as $f=2.45Hz$. Top panel shows the initial setting of fluid markers and the immersed elastic boundary. Red dots are fluid markers spread in space where $0cm\leq z\leq16cm$, and blue dots are fluid markers spread in space

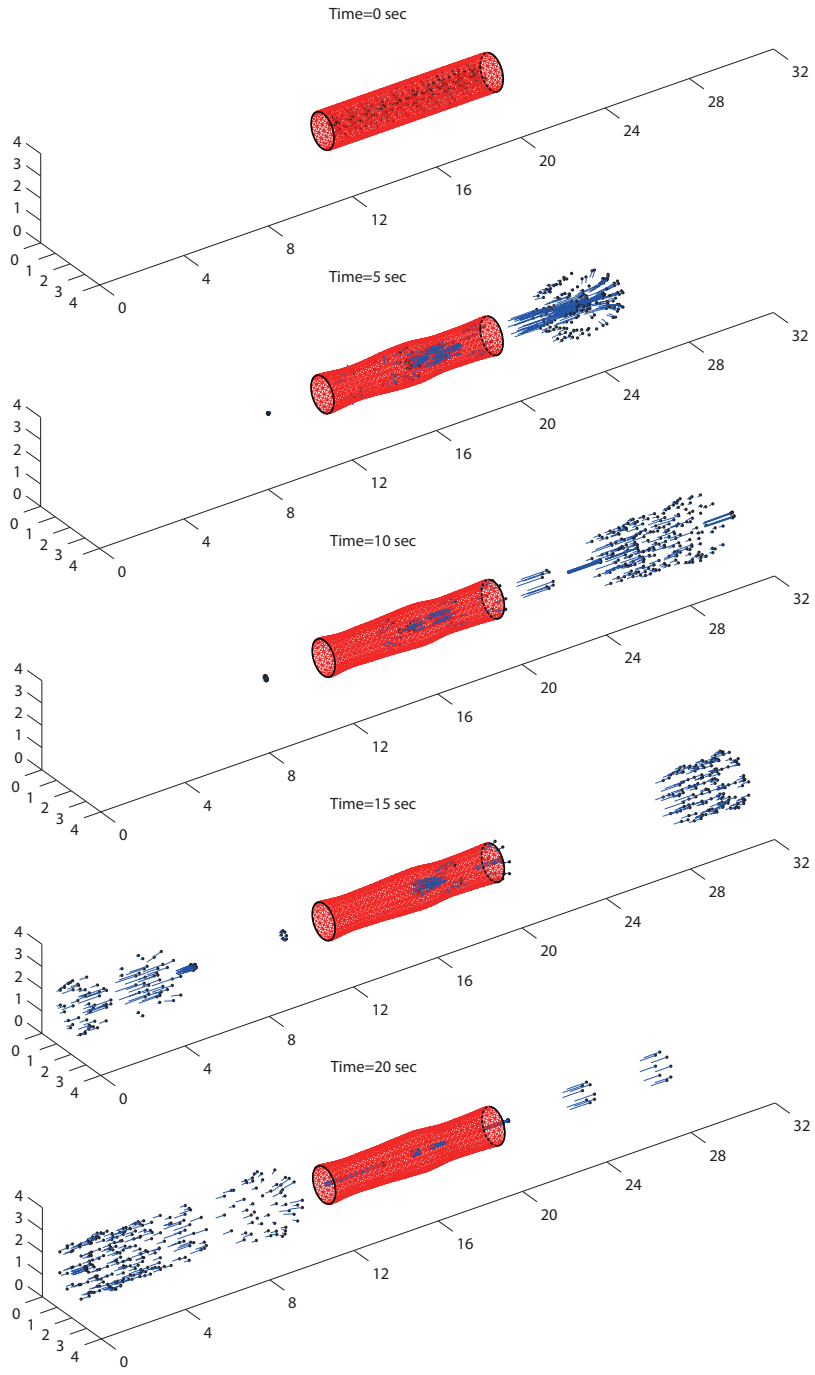

Figure 9: A positive flow at $f=4Hz$. Snapshots are taken at five different times showing the motion of fluid-tube interaction over $20sec$. Fluid markers are initially spread inside the open tube. The current position of fluid markers is represented by the head of a trajectory and the trajectory traces the fluid markers at previous time. Note that the fluid domain is periodic so that fluid markers leaving the domain on the right side of the tube will reappear on the left side of the fluid domain.

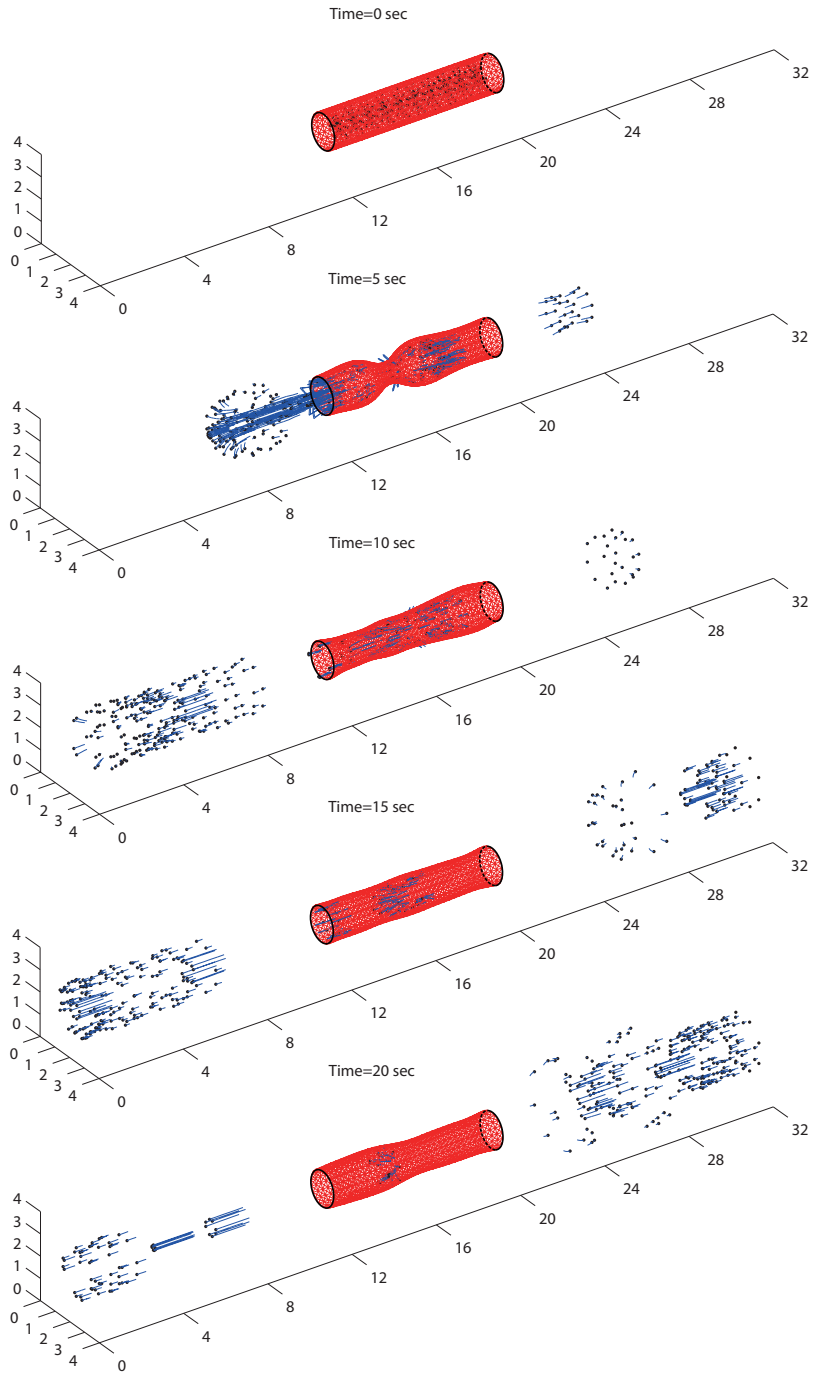

Figure 10: A negative flow at $f=2.45Hz$. Snapshots are taken at five different times showing the motion of fluid-tube interaction over $20sec$. Fluid markers are initially spread inside the open tube. The current position of fluid markers is represented by the head of a trajectory and the trajectory traces the fluid markers at previous time. Note that the fluid domain is periodic so that fluid markers leaving the domain on the left side of the tube will reappear on the right side of the fluid domain.

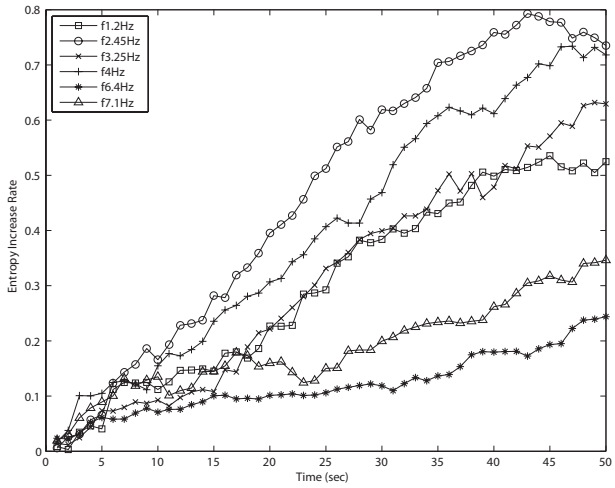

Figure 11: Time evolution of the entropy increase rate for a range of pumping frequencies.

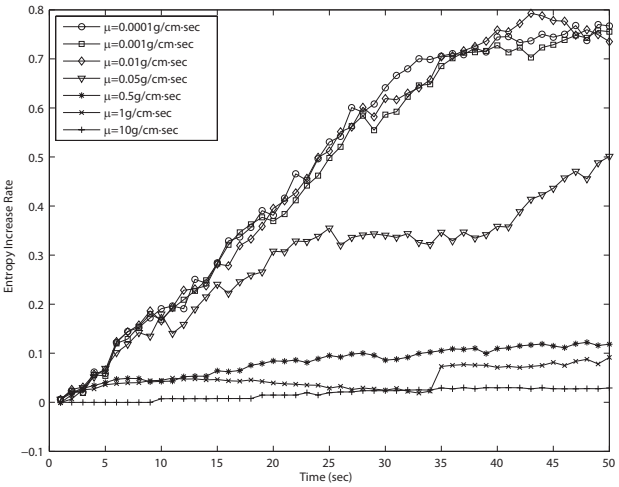

Figure 12: Time evolution of the entropy increase rate with various fluid viscosity. The pumping frequency is fixed as $f=2.45Hz$.

where $16cm \leq z \leq 32cm$. Second panel shows mixing state at $t=50sec$ when fluid viscosity is $\mu = 0.0001g/cm\cdot sec$. This is the case where the fluid is mixing efficiently, see Fig. 12 for the entropy rate. Bottom panel shows mixing state at $t=50sec$ when fluid viscosity is $\mu = 10g/cm\cdot sec$. This is the case where the fluid stays near the initial position, see Fig. 12 for the entropy rate. As expected, the pumping part of the tube in high viscous fluid compresses less and releases less because of viscous resistance so that fluid markers around the tube do not move much. This gives the same effect that the small pumping amplitude produces inactive fluid motion, see Fig. 7.

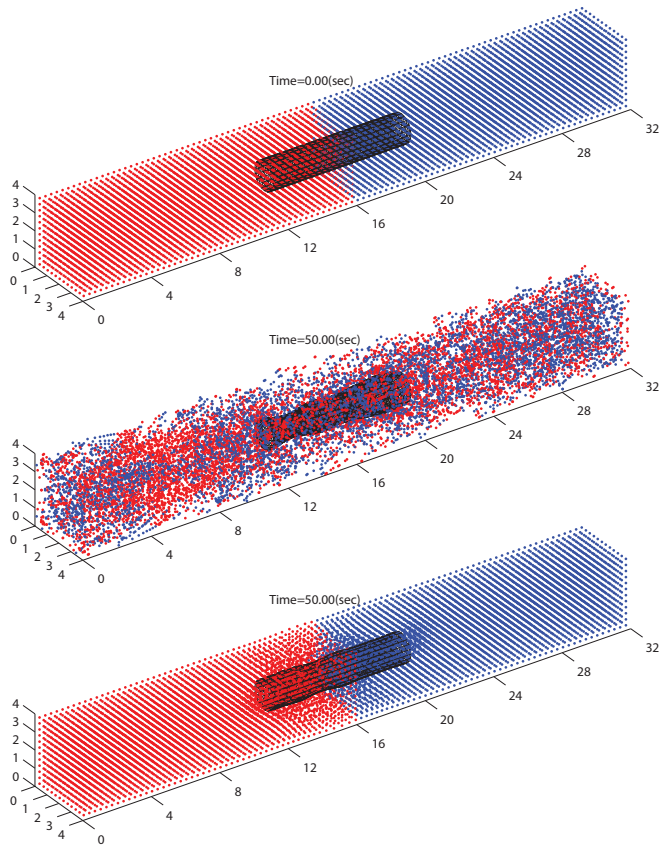

Figure 13: The mixing performance at $f=2.45Hz$ with two different viscosities. Top panel shows the initial setting of fluid markers and elastic boundary. Red dots are fluid markers spread in space where $0cm\leq z\leq 16cm$, and blue dots are fluid markers spread in space where $16cm\leq z\leq 32cm$. Second panel shows mixing state at $t=50sec$ given that fluid viscosity is $\mu=0.0001g/cm\cdot sec$. Bottom panel shows mixing state at $t=50sec$ given that fluid viscosity is $\mu=10g/cm\cdot sec$.

4 Summary and conclusion

In this paper, we have presented simulations of three-dimensional valveless pumping in an open system. We compared the typical IB method with the volume conserved IB method in three aspects: volume conservation of a circle in two-dimensional space, the velocity vector field near a tube surface in three-dimensional space, and the structure of the pumping part of the tube. Volume loss through a leaky boundary is a weak point of the typical IB method, in particular, for the problems of which the volume conservation is important. A new difference operator $\boldsymbol{D}$ introduced in the volume conserved IB method helps to prevent the generation of spurious velocities near the structure and helps to maintain the tension between linear springs near the pumping part of the tube where the force is applied, which result in keeping the same volume during simulation.

We showed that a variety of parameters such as pumping frequency, compression

duration, and pumping amplitude affect the direction of net flow and its magnitude. We also showed that for a fixed pumping frequency and compression duration different values of the pumping amplitude do not change the direction of net flow but change only the flow magnitude.

In order to investigate the mixing performance we introduced the Shannon entropy increase rate. It is observed that VP systems tend to get high entropy increase rate when the magnitude of average net flow is large. Fluid mixing by periodic pumping is very efficient at the high Reynolds number but it is of no effect at the low Reynolds number. This implies that at the low Reynolds number different approaches other than valveless pumping are necessary to increase mixing performance. Potential candidates are using beating cilia or rotating flagella.

Acknowledgments

Jung's work was supported by a Basic Science Research Program through the National Research Foundation of Korea (NRF) funded by the Ministry of Education, Science and Technology (No. 2009-0077511). S. Lim acknowledges the support from Charles Phelps Taft Research Center, University of Cincinnati. Lee's work was supported by the Korea Student Aid Foundation (KOSAF) grant funded by the Korea government (MEST) (No. S2-2009-000-00256-1).

References

[1] D. Auerbach, W. Moehring,and M. Moser, An analytic approach to the Liebau problem of valveless pumping, Cardiovasc. Eng. Int. J., 4 (2004), 201-207.
[2] M. Baltussen, P. Anderson, F. Bos, J.D. Toonder, Inertial flow effects in a micro-mixer based on artificial cilia, Lab on a Chip, 9 (2009), 2326-2331.
[3] A. Borzi and G. Propst, Numerical investigation of the Liebau phenomenon, Z. Angew. Math. Phys., 54 (2003), 1050-1072.
[4] T. Bringley, S. Childress, N. Vandenberghe, and J. Zhang, An experimental investigation and a simple model of a valveless pump, Phys. Fluids, 20 (2008), paper 033602.
[5] F.C. Donders, Physiologie des menschen, S. Hirzel, Leipzig, 1859.
[6] A.I. Hickerson and M. Gharib, On the resonance of a pliant tube as a mechanism for valveless pumping, J. fluid Mechanics., 555 (2006), 141-148.
[7] A.I. Hickerson, D. Rinderknecht, M. Gharib, Experimental study of the behavior of a valveless impedance pump, Experiments in Fluids, 38 (2005), 534-540.
[8] E. Jung, S. Lim, W. Lee, and S. Lee, Computational models of valveless pumping using the immersed boundary method, Comput. Methods Appl. Mech. Engrg., 197 (2008), 2329-2339.
[9] E. Jung, A mathematical model of valveless pumping: a Lumped model with time-dependent compliance, resistance, and inertia, Bull. Math. Biol., 69 (2007), 2181-2198.
[10] E. Jung, C.S. Peskin, Two-dimensional simulations of valveless pumping using the immersed boundary method, SIAM J. Sci. Comput., 23 (2001), 19-45.
[11] E. Jung, 2-D simulations of valveless pumping using the immersed boundary method, Ph.D. Thesis, Courant Institute, New York University, 1999.

[12] P.J. Kilner, Formed flow, fluid oscillation and the heart as a morphodynamic pump, Eur. Surg. Res., 19 (1987), 89-90.
[13] W. Lee, S. Lim, and E. Jung, Movies of the three-dimensional simulations of valveless pumping on an open elastic tube, `http://math.konkuk.ac.kr/junge/OpenVp3d.html`, 2010.
[14] W. Lee, E. Jung, and S. Lee, Simulation of valveless pumping in an open elastic tube, SIAM J. Sci. Comput., 31 (2009), 1901-1925.
[15] G. Liebau, Die Bedeutung der Tragheitskrafte fur die Dynamik des Blutkreislaufs, Z. Kreislaufforsch, 46 (1957), 428-438.
[16] G. Liebau, Die Stromungsprinzipien des Herzens, Z. Kreislaufforsch, 44 (1955), 677-684.
[17] G. Liebau, Uber ein Ventilloses Pumpprinzip, Naturwissenschsften, 41 (1954), 327-328.
[18] S. Lim and E. Jung, Three-dimensional simulations of a closed valveless pump system immersed in a viscous fluid, SIAM J. Sci. Comput., 70 (2010), 1999-2022.
[19] C.G. Manopoulos, D.S. Mathioulakis, S.G. Tsangaris, One-dimensional model of valveless pumping in a closed loop and a numerical solution, Phys. Fluids, 18 (2006), 017106.
[20] M. Moser, J.W.Huang, G.S. Schwarz, T. Kenner, A. Noordergraaf, Impedance defined flow, generalisation of William Harvey's concept of the circulation - 370 years later, Int. J. Cardiovasc. Med. Sci., 71 (1998), 205-211.
[21] J.T. Ottesen, Valveless pumping in a fluid-filled closed elastic tube-system: one-dimensional theory with experimental validation, J. Math. Biol., 46 (2003), 309-332.
[22] C.S. Peskin, The Immersed Boundary Method, Acta Numerica, (2002), 1-39.
[23] C.S. Peskin and D.M. McQueen, Fluid dynamics of the heart and its valves, in Case Studies in Mathematical Modeling: Ecology, Physiology, and Cell Biology, H. G. Othmer, F. R. Adler, M. A. Lewis, and J. C. Dallon, eds., Prentice-Hall, Englewood Cliffs, NJ, (1996), 309-337.
[24] C.S. Peskin, D.M. McQueen, A general method for the computer simulation of biological systems interacting with fluids, Symposia of the Society for Experimental Biology, 49 (1995), 265-276.
[25] C.S. Peskin, B.F. Printz, Improved volume conservation in the computation of flows with immersed elastic boundaries, J. Comput. Phys. 105 (1992), 33-46.
[26] D. Rinderknecht, A.I. Hickerson, M. Gharib, A valveless micro impedance pump driven by electromagnetic actuation, J. Micromech. Microeng., 15 (2005), 861-866.
[27] S. Shin and H. Sung, Three-dimensional simulation of a valveless pump, Int. J. Heat Fluid Flow, 31 (2010), 942-951.
[28] H. Thomann, A simple pumping mechanism in a valveless tube, J. Appl. Math. Phys., 29 (1978), 169-177.
[29] S. Timmermann and J.T. Ottesen, Novel characteristics of valveless pumping, Phys. Fluids, 21 (2009), 053601.
[30] L. Zhu and C.S. Peskin, Simulation of a flapping flexible filament in a flowing soap film by the immersed boundary method, J. Comput. Phys., 179 (2002), 452-468.
[31] D.P. Zipes, P. Libby, R.O. Bonow, and E. Rraunwald, Braunwald's Heart Disease: A Textbook of cardiovascular medicine, Vol 2, 7th Edition, W.B. Saunders Company, (2004), 1311-1328.